ORIGINAL ARTICLE

Plane grind-hardening distortion analysis and the effect to grind-hardening layer

Ying Zhang · Peiqi Ge · Wenbo Be

Abstract The high temperature and grinding force in grind hardening induce workpiece distortion that increases the magnitude of grinding to make the workpiece concave. The workpiece distortion also affects the grinding force, grinding heat flux, and grind-hardening depth distribution. The paper uses FE thermo-mechanical coupling model to simulate the thermal distortion in plane grind-hardening. Workpiece distortion, stress, and strain at different moments are calculated out and analyzed for different workpiece sizes. The calculated workpiece distortion is verified through the measured workpiece contour and the hardening layer distribution by experiment.

Keywords Grind hardening · Thermal distortion · FE

1 Introduction

Grind hardening was firstly introduced by Brinksmeier and Brockhoff in 1994 [1]. The process uses the heat generated in grinding to get surface hardening. Grind hardening has much been studied due to its manufacturing integration superiority and reduction in energy consumed. K. Salonitis [2], G. C. Wang [3], T. Nguyen [4], and J. H. Zhang [5] used finite element analysis (FEA) to study the grind-hardening temperature and combined with heat theory to predict the grind-hardening depth. In fact, the depth distribution of grinding–hardening layer

is not uniform. L. Zhang divided the workpiece after grind hardening into the incising area, central area, and cut-out area through analyzing the uneven grinding–hardening depth distribution through experiment [6]. Z. J. Zhuang also studied the grinding depth uniformity through grind-hardening experiment [7].

High grinding temperature and grinding force induce the workpiece distortion that caused the workpiece surface concave. The workpiece distortion in grinding has been calculated by FEA in many studies [8–10]. In grind-hardening, the distortion can also be calculated by FEA. M. F. Zäh established the thermo-metallurgical model and used FEA to simulate the part distortion in grind hardening [11]. B. Kolkwitz identified and analyzed the part distortion resulting from grind-hardening process using computer-based methods [12]. In both studies, the simulated distortion was compared with the measured result. But the distortion in grind hardening varies in different time. The distortion in grind-hardening process induces the variation of grinding force and the heat flux and finally, impacts of the grind-hardening layer distribution. The workpiece contour and the grind-hardening depth distribution after grind hardening are shown in Fig. 1. The top horizontal contour is the machined ideal surface. Beneath the ideal surface is the concave contour for actual machined surface. Beneath the actual surface is the hardening layer distribution. There is a relationship among the three contours.

The paper uses coupled thermal–mechanical finite element analysis to simulate the grind-hardening process to get distortion, stress, and strain for different workpiece sizes. The calculated distortion is compared with the measured workpiece contour by experiment. The relationship between distortion and grind-hardening depth distribution is also analyzed through the measured hardening depth distribution by experiment.

Y. Zhang (✉)
School of Mechanical and Electrical Engineering, Shandong Jianzhu University, Jinan 250101, China
e-mail: girlcheryl@163.com

P. Ge · W. Be
School of Mechanical Engineering, Shandong University, Jinan 250061, China
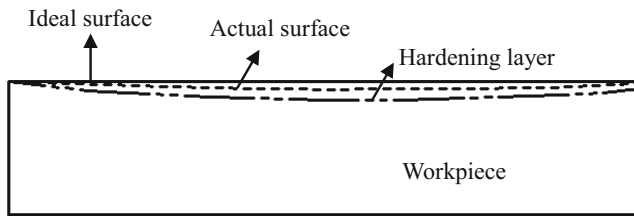
Fig. 1 The workpiece ideal surface contour, actual contour, and hardening layer distribution after grind hardening

2 Grind-hardening experiment

Grind-hardening experiment uses single-pass grinding on a CNC MKL7120X6 without grinding fluids. The grinding parameters are shown in Table 1. Due to the good stiffness of grinding machine, the distortion among machine grinding, wheel–workpiece, and the wear of the grinding wheel is neglected. The workpiece material is initially annealed 40Cr and the overall size is $80 \times 10 \times 10$ mm, $80 \times 10 \times 50$ mm, and $80 \times 10 \times 100$ mm. Grinding forces are measured on a piezo-electric dynamometer-YDXMIII97 and amplified with a charge amplifier. The workpiece holding mode is shown in Fig. 2. Through tightening the bolt, the side of the workpiece is fixed by the clamp. The grinding force under different feed rates and different grinding depths is collected as shown in Table 2. The surface contour is measured by lever-type dial indicator after the workpiece is finished. Due to the concave surface contour of workpiece, the concavity is defined as the height difference between the highest and the lowest points. The hardness is measured by MH-6 hardness tester. When hardness of the workpiece tested area reaches 600 HV, then the grind hardening occurs as the 40Cr hardness limit of 600 HV. So, the hardening depth distribution curve can be obtained by measuring the hardness at different locations along the workpiece length.

3 Grind-hardening distortion numerical analysis

3.1 Coupled thermal–mechanical analysis

The workpiece distortion is simulated by coupled thermal–mechanical finite element method through ANSYS software.

Table 1 Grinding parameters

Grinding condition	Parameters value
Grinding wheel	WA60L6V
Linear velocity of grinding wheel (m/s)	30
Feed velocity (mm/s)	10, 20, 30
Grinding depth (mm)	0.05, 0.1, 0.15
Cooling method	Dry grinding
Grinding mode	Down grinding

The load is grinding temperature and grinding force. The first analysis step is finite element analysis for grinding temperature. The second step is mechanical finite element analysis for loading temperature and force together.

The grinding power consumption of wheel spindle can be expressed as:

$$P_c = \frac{F_t(v_s \pm v_w)}{bl_c} \tag{1}$$

where F_t is the grinding tangential force, V_s is the grinding wheel speed, V_w is the workpiece feed speed, b is the grinding wheel width and l_c is the contact length.

Almost all grinding energy generates heat in the grinding contact area. The total heat flux is mainly transferred to workpiece and grinding wheel. The partition ratio ε is defined as the fraction of the generated heat that enters the workpiece calculated by: [13].

$$\varepsilon = \frac{1}{1 + \left[\dfrac{Av_s}{v_w}\right]^{1/2} \left[\dfrac{(k\rho c)_c}{(k\rho c)_w}\right]^{1/2}} \tag{2}$$

where A is the ratio of the abrasive actual contact area with workpiece to grinding wheel geometric contact area with workpiece, k is the heat transfer coefficient, ρ is the density, C is the specific heat, subscript c is for the grinding wheel, and subscript w is for the workpiece.

Through the total heat flux q and heat partition ratio ε, the part heat flux into the workpiece can be calculated by:

$$q_w = \varepsilon q \tag{3}$$

After the heat conducts into the workpiece, it forms a temperature gradient. The model to analyze temperature is that grinding heat is treated as a banding heat source moving on a semi-infinite surface.

In the heating and cooling process, material absorbs or releases heat caused by phase transformation. The phase transformation latent heat affects grinding temperature.
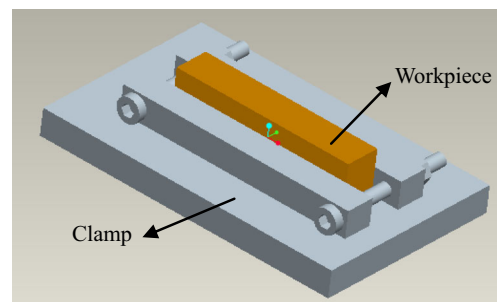

Fig. 2 Workpiece holding mode

Table 2 Grinding force by experiment

Number	Size W×D×H (mm)	a_p (mm)	v_w (mm/s)	v_s (m/s)	F_t (N)	F_n (N)
1	80×10×10	0.05	10	30	70	201
2	80×10×50	0.05	10	30	52	152
3	80×10×100	0.05	10	30	48	126
4	80×10×10	0.1	20	30	106	267
5	80×10×50	0.1	20	30	103	240
6	80×10×100	0.1	20	30	93	233
7	80×10×10	0.15	30	30	110	320
8	80×10×50	0.15	30	30	107	257
9	80×10×100	0.15	30	30	105	250
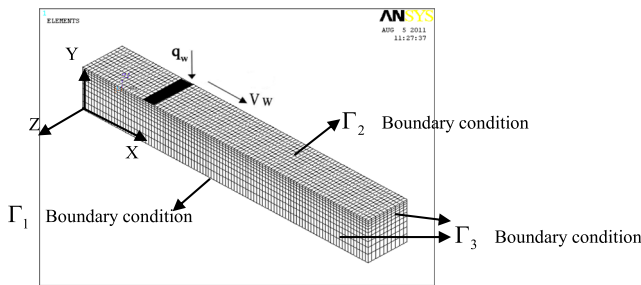
Fig. 3 Modeling and meshing

**Fig. 4** Grinding isothermal phase diagram for 4#

1-1280℃; 2-900℃; 3-500℃; 4-300℃; 5-200℃
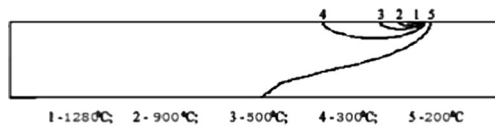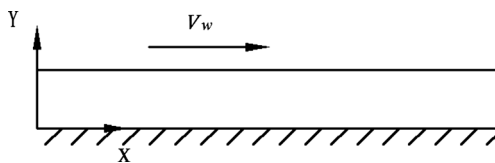
Fig. 5 Displacement constraint position

Thus, the latent heat is treated as the interior heat source in finite element calculation here. In thermal–mechanical finite element analysis, the phase transformation also makes the material expand and affects stress–strain relationship. So, the material uses coefficient of cubical thermal expansion considering the phase transformation in finite element analysis.

The three-dimensional workpiece model is established and meshed as shown in Fig. 3. The closer the grid is, the more computation time is needed. In grind hardening, the heating time is short, so the high temperature concentrated on the workpiece surface. To save calculated time, the model is
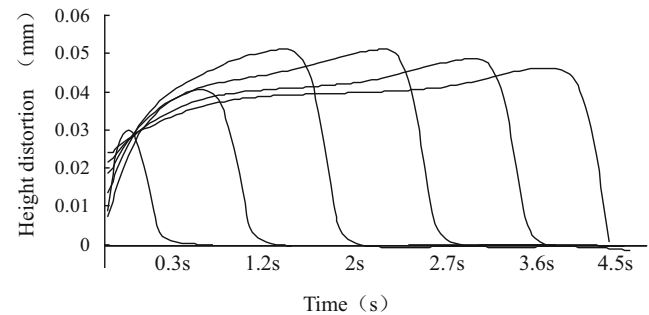
Fig. 7 Distortion of Y direction at different moment for 4#

Fig. 6 Distortion cloud photograph of Y direction at loading 1.61 s for 4#
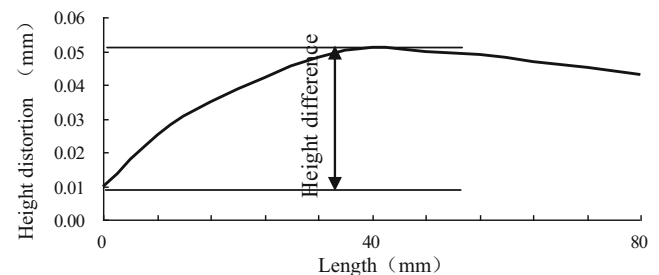
Fig. 8 Height distortion difference in grinding arc for 4#

Table 3 The distortion difference of height

Number	Size L×W×H (mm)	Height difference for convex distortion (mm)	
		Load grinding force	Unload grinding force
1	80×10×10	0.038	0.0382
2	80×10×50	0.0355	0.0357
3	80×10×100	0.035	0.0351
4	80×10×10	0.0453	0.0454
5	80×10×50	0.0442	0.0443
6	80×10×100	0.044	0.0441
7	80×10×10	0.03	0.031
8	80×10×50	0.026	0.0261
9	80×10×100	0.025	0.0251

divided into 10 according to the grid close near the workpiece surface and coarse far away from the surface in the height direction, 10 in the width direction and 100 in the length direction.

Three kinds of boundary condition are loaded. Room temperature is applied to Γ_1 boundary. The heat flux q_w calculated by Eq. 3 is applied to Γ_2 boundary. The air heat transfer coefficient is applied to Γ_3 boundary. The workpiece surface is treated as adiabatic due to the short grinding contact time and the poor conductivity of air. The grinding isothermal phase diagram for simulated temperature is shown in Fig. 4 for 4#. The highest temperature is 1280 °C in the grinding contact arc. The temperature decreases quickly under the workpiece surface.

The second step is workpiece distortion analysis by coupled thermal–mechanical finite element method. The coupled analysis uses sequential coupled method through thermal elastic–plastic finite element method. The distortion is calculated by loading grinding temperature by simulation and grinding force by experiment. The displacement is exerted on the bottom side of the model to simulate the workpiece holding mode as Fig. 5. The height distortion cloud photograph is shown in Fig. 6 at loading time 1.8 s for 4#. The processed

surface is convex and the maximum occurs in the grinding arc zone. The unprocessed area is affected slightly. Distortion at different loaded time along the workpiece length is shown in Fig. 7 for 4#. The height distortion is minimal in the beginning process. As the grinding temperature is raised, the height distortion is increased and the maximum occurs in two thirds of the workpiece length. The distribution of maximum distortion at different grinding time along the workpiece length is drawn in Fig. 8. The height difference between the highest distortion point and the lowest distortion point can reflect the degree of distortion. Actually, the convex distortion is removed by the grinding wheel in the process, so the workpiece is concave in contradiction to the convex distortion after processing.

The influence of grinding force and workpiece size to the workpiece distortion are analyzed through loading or unloading grinding force in the simulation. The simulated height difference for all workpiece with variant machine parameter is shown in Table 3. The result analysis is as follows:

(1) The concave distortion decreases accompanying the increase of the workpiece height with same machine parameter. The reason may be the grinding force measured by the experiment decreasing as the workpiece height increases. The decreasing grinding force decreases the grinding temperature. The decreasing temperature decreases the distortion.

(2) Loading grinding force has little effect on the distortion. The distortion is mainly caused by heat.

3.2 Grinding thermal stress and strain analysis

The stress and strain inside the model are calculated by ANSYS. The stress distribution curve along the workpiece length direction is shown in Fig. 9 at loading time 1.8 s for 4#. The shadow part is in grinding arc. It is obvious that the machined surface is tensile stress in X and Z directions but compressive stress in Y direction. The stress in the unprocessed area is little. The concentrated compressive stress is found in the grinding

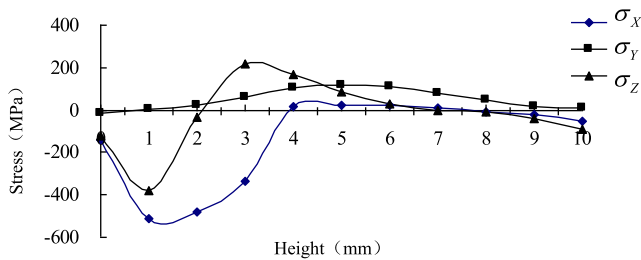**Fig. 9** Surface stress distribution for height of 10 mm at 1.8 s
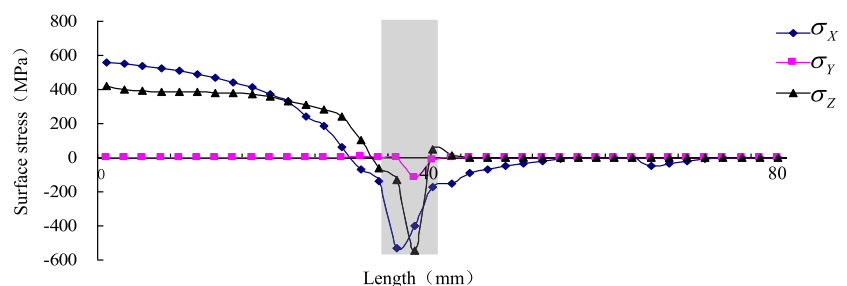
Fig. 10 Depth stress distribution under grinding contact zone at 1.61 s for 7#

arc, which is caused by the high temperature in grinding arc accompanying the lower yield stress. When the top compressive stress is above the yield stress, the plastic distortion occurs in the grinding arc.

The three-direction stress below the workpiece surface at loading time 1.8 s in grinding arc for 4# is shown in Fig. 10. Compressive stress occurs in the workpiece surface. As the workpiece depth increases, the tensile stress occurs and goes little. So, the farther away from the workpiece surface, the lesser the stress is.

The elastic strain distribution at loading 1.8 s for 4# is shown in Fig. 11a. The processed area has an elastic strain in the depth direction and the maximum occurs at the grinding start of the workpiece. The plastic strain distribution at loading 1.8 s for 4# is shown in Fig. 11b. The machined workpiece surface has plastic strain especially in the grinding arc, which can be explained by the stress analysis aforementioned.

The elastic and plastic strain distribution at loading 1.8 s for 6# is shown in Fig. 12 comparing with 4#. Plastic strain similarly occurs in the surface of the workpiece. The elastic strain concentrated under the plastic strain area. But the strain is little at the bottom of the workpiece. It can be concluded that the higher the workpiece is, the lesser the bottom of the workpiece is affected. The plastic and elastic strains induce the workpiece distortion together.

Figure 13 shows the three-direction stress distribution in constraint position at loading 1.61 s for 4#, 5#, and 6#. Similar stress distribution occurs for 4# and 5#. Along the workpiece

length, the beginning of the workpiece is compressive stress and the end of the workpiece is tensile stress. The stress of 4# is distinctly greater than 5# and 6#. Based on beam bending theory, thinner workpiece is easily bended; 4# is the thinnest workpiece, so its bend is the greatest. Similar rule is applicable for the other experiment result. The bend is balanced by the constraint force to realize the displacement; otherwise, slide occurs at constraint position. So, the thinnest workpiece 4# has the maximum stress in the constraint position comparing with 5# and 6#.

4 The comparison between experiment and simulation for workpiece surface contour and hardening layer distribution analysis

The measured surface contour is shown in Fig. 14 corresponding to Table 1. The vertical ordinate zero is the highest point of workpiece contour and another curve is the distribution of hardening layer depth. Both the workpiece contour and the hardening layer distribution are uneven. In the grinding beginning, the contour concavity and the depth of hardening layer are both little and got deeper later. The analysis for the distribution of workpiece contour and grind-hardening depth in Fig. 14 is as follows: The grinding force is small and the accumulated heat flux is insufficient in the grinding beginning, so the concavity and hardening depth are little. Later, the heat flux increases grinding temperature, so the distortion and hardening depth goes deeper.

The comparison of calculated largest distortion and the measured concavity in Fig. 10 are shown in Table 4. The experimental distortion result varies greater than the simulation. The largest concavity occurs in the workpiece height of 10 mm for 1#, 4#, and 7# and there measured concavity is much larger than the calculated distortion result. Other workpiece's measured concavity is close to the calculated result. The concavity is larger in 2#, 5#, and 8# for the height of 50 mm than 3#, 6#, and 9# for the height of 100 mm. The
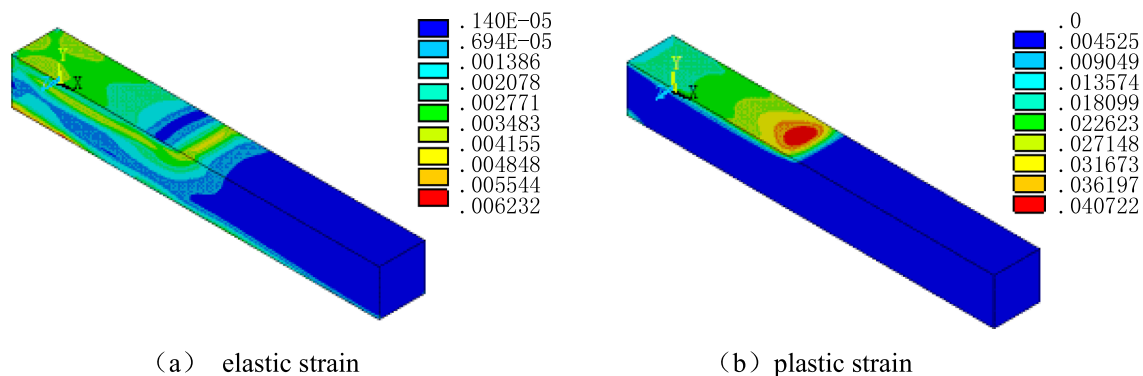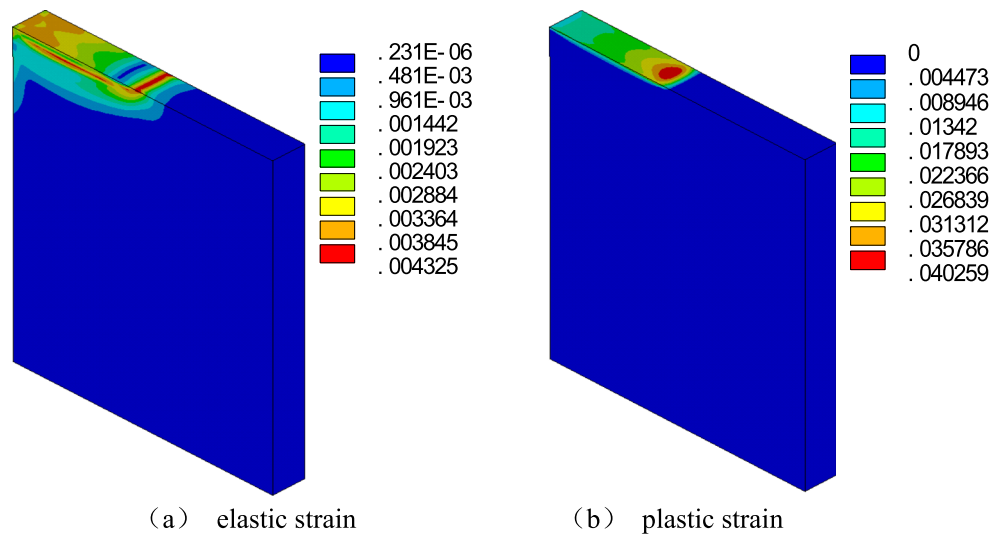

（a） elastic strain

（b） plastic strain
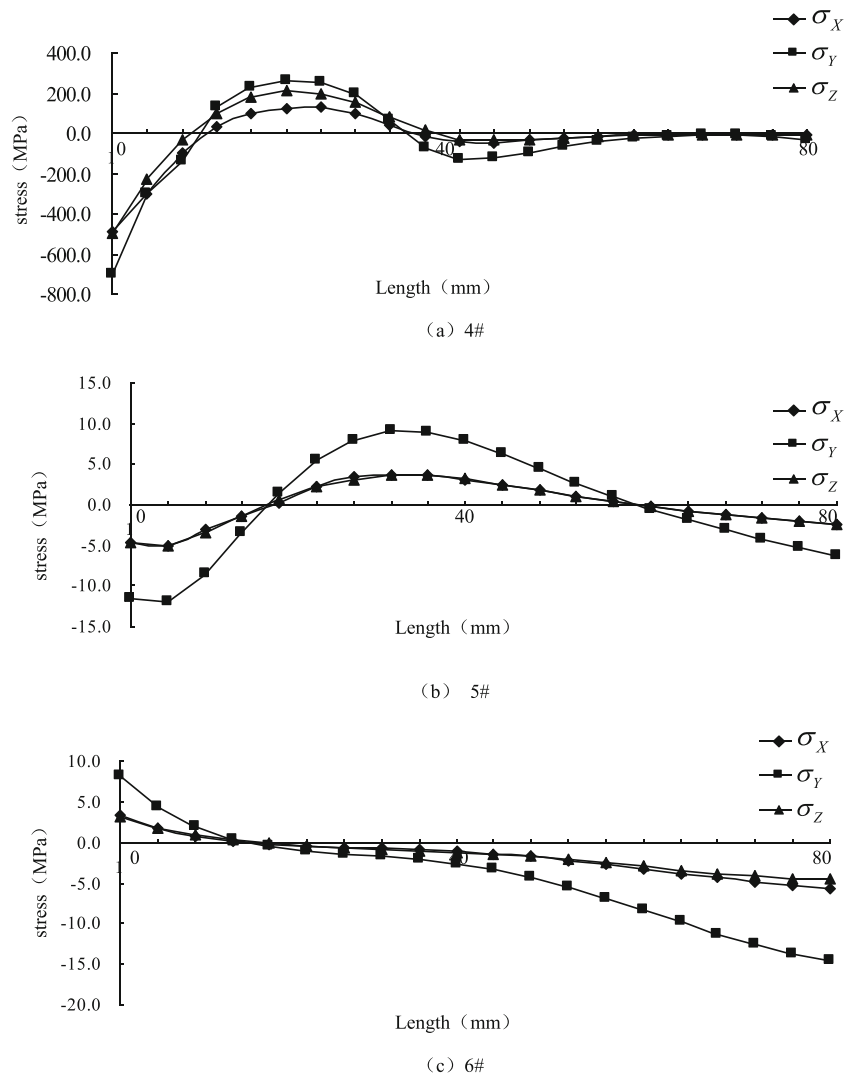
Fig. 11 Strain distribution for 4# at 1.8 s

Fig. 12 Strain distribution for 6#
at 1.8 s

（a） elastic strain

（b） plastic strain

Fig. 13 The stress distribution on
restraint position at 1.61 s
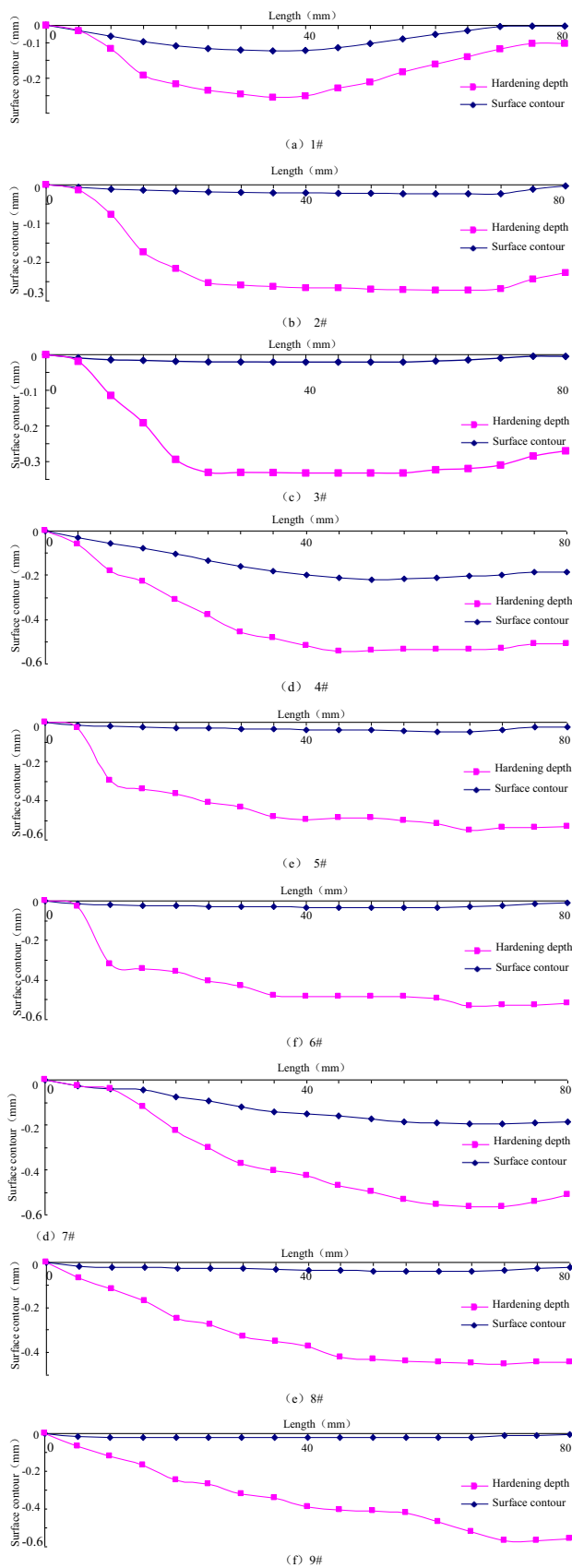

（a） 4#

（b） 5#

（c） 6#

Fig. 14 Surface contour and hardening depth distribution

Table 4 The comparison between experiment and simulation

Number	Size L×W×H (mm)	Height difference for distortion (mm)		Maximum hardening depth (mm)
		Experiment	Simulation	
1	80×10×10	0.13	0.0382	0.25
2	80×10×50	0.03	0.0357	0.28
3	80×10×100	0.035	0.0351	0.34
4	80×10×10	0.21	0.0454	0.57
5	80×10×50	0.08	0.0443	0.55
6	80×10×100	0.05	0.0441	0.54
7	80×10×10	0.2	0.031	0.58
8	80×10×50	0.05	0.0261	0.46
9	80×10×100	0.03	0.0251	0.52

analysis is as follows: In the simulation, the workpiece constraint position is imposed as Fig. 5. The workpiece distortion is prone to occur in the thinner workpiece of 10 mm for 1#, 4#, and 7# based on beam bending theory as mentioned before. The distortion increases the grinding depth and grinding force that leads to uneven surface contour and grinding–hardening depth distribution. So, it can explain why the tested grinding forces for 1#, 4#, and 7# are larger than other. When the workpiece height increases, the workpiece distortion decreases. That may explain why the calculated concavity is close to the measured result for the workpiece height of 50 and 100 mm. Other differences between experiment and simulation result may be that the temperature numerical analysis uses uniform heat flux. Actually, the grinding force and the heat flux change along with the grinding distortion.

5 Summary

The grinding heat and force induce the workpiece distortion in plane grind hardening that makes the workpiece contour concave. The stress and strain concentrate on the workpiece surface especially in the grinding arc zone. The surface stress exceeds the yield stress to get plastic deformation. Faraway from the surface, the deformation is elastic. The distortion is mainly induced by grinding heat. Grinding force has little effect to the distortion. The overall distortion variation rule is based on the grinding parameter and the workpiece size.

From the comparison of workpiece distortion between the experiment and simulation, the result is close for the height of 50 and 100 mm and considerably different for the height of 10 mm. The reason is that the thinner the workpiece is, the more severe the workpiece distortion occurs. The distortion changes the grinding magnitude and affects grinding–hardening depth distribution. So, the workpiece distortion and grinding–hardening depth distribution are correlated and affected

by grinding parameter, workpiece size, workpiece constraint condition, etc. The following work will study the regularities among them.

References

1. Brinksmeier E, Brockhoff T (1996) Utilization of grinding heat as a new heat treatment process. CIRP Ann Manuf Technol 45(1):283–286
2. Salonitis K, Chondros T, Chryssolouris G (2008) Grinding wheel effect in the grind-hardening process. Int J Adv Manuf Technol 38(1–2):48–58
3. Wang GC, Liu JD, Pei HJ (2006) Study on forming mechanism of surface hardening in two-pass grinding 40Cr steel. Key Eng Mater 304:588–592
4. Nguyen T, Zarudi I, Zhang LC (2007) Grinding-hardening with liquid nitrogen: mechanisms and technology. Int J Mach Tools Manuf 47(1):97–106
5. Zhang JH, Ge PQ, Tien-chien J, Zhang L (2009) Experimental and numerical studies of AISI1020 steel in grinding-hardening. Int J Heat Mass Transf 52:787–795
6. Zhang L (2006) Theory analysis and experimental investigation for single-pass plane grinding-hardening technology, Shandong University doctoral thesis
7. Zhuang ZJ (2011) The study for grinding-hardening layer and uniformity, JiMei University Master thesis
8. Kagiwada T, Kanauchi T (1985) Three-dimensional thermal deformation and thermal stress in workpieces under surface grinding. J Therm Stresses 8(3):305–318
9. Nishihara T, Okuyama S, Kawamura S, Hanasaki S (1993) Study on the geometrical accuracy in surface grinding-thermal distortion of workpiece in traverse grinding. JSPE 59:1145–1150
10. Tsaia HH, Hocheng H (2002) Prediction of a thermally induced concave ground surface of the workpiece in surface grinding. J Mater Process Technol 122:148–159
11. Zäh MF, Brinksmeier E, Heinzel C (2009) Experimental and numerical identification of process parameters of grind-hardening and resulting part distortions. Prod Eng 3(3):271–279
12. Kolkwitz B, Foeckerer T, Huntemann JW (2011) Identification and analysis of part distortion resulting from grind-hardening process using computer-based methods, Proceedings of the 3rd international conference on distortion engineering 2011: 499–506
13. Lavine AS (2000) An exact solution for surface temperature in down grinding. Int J Heat Mass Transf 43(24):4447–4456